STEWARD-1056
Fermilab Library
0 1160 0013485 2
NOTE TO
NAME LOCATION
RETURN TO TERM LIBRARY

PREPRINTS

of the

STEWARD OBSERVATORY

THE UNIVERSITY OF ARIZONA
TUCSON, ARIZONA 85721 U.S.A.

No. 1056

A RADIATIVE-HYDRODYNAMICAL STUDY OF ACCRETION-DISK CORONAE IN BRIGHT LOW-MASS X-RAY BINARIES[1]

Gregory J. Zylstra[2] and Fulvio Melia[3†]

[2]Department of Physics, University of Arizona
[3]Department of Physics and Steward Observatory, University of Arizona

MELA
JUN 26 1992

Submitted to the Editor of the Astrophysical Journal on June 12, 1992.

---

[1]Contribution No. 92-25 of the University of Arizona Theoretical Astrophysics Program.
[†]Presidential Young Investigator and Alfred P. Sloan Fellow.

ATAP-92-25

Abstract

We present in detail the results of our two-dimensional, fully self-consistent radiative-hydrodynamical simulation of an accretion disk corona in low-mass X-ray binaries radiating at half the Eddington limit. The corona is comprised of two main regions, separated roughly by the radius at which the evaporated plasma first attains escape velocity. The inner portion is highly variable, and oscillates quasi-periodically on a dynamic time scale, whereas the outer corona is more stable with the gas rising to form a density sheath that merges into a wind at larger radii. Observationally, the corona can signficantly alter the appearance of the central source since it enhances the flux by as much as 100% when the neutron star is seen directly, while it suppresses the observed flux by an order of magnitude deep within its shadow.

Subject headings: radiative transfer—stars: accretion—stars: binaries—stars: coronae—stars: neutron

1. Introduction

We have previously introduced a model for accretion disk coronae (ADCs) in low mass X-ray binaries (LMXRBs) that for the first time self-consistently accounts for both the dynamical and radiative aspects of the evaporated plasma (Melia, Zylstra & Fryxell 1991, MZF). Such a detailed treatment is necessary because of the role played by ADCs in shaping the observational characteristics of these systems. For instance, there is no doubt that the X-ray source in the eclipsing binaries 4U 2129 + 47 and 4U 1822 − 37 is diffused by a large, extended corona (White and Holt 1982; McClintock et al. 1982). In addition, some X-ray burst profiles may result from the scattering of X-rays by a time-dependent, burst-induced coronal flow along the line of sight (Melia 1987; Melia & Zylstra 1992; Melia, Zylstra & Fryxell 1992). And finally, ADCs may be the regions producing the iron emission lines observed in many LMXRBs (White, Peacock, and Taylor 1985). These features, among others, provide an invaluable diagnostic tool for probing the nature of hot plasmas in cosmic X-ray sources, particularly with regard to the still poorly understood accretion flow geometry.

Studies of ADCs based on the assumption of an inner, hydrostatic region with a Gaussian density distribution, and a wind in the outer region, do not self-consistently account for the shadowing of the disk surface by the inner corona and the contribution to the heating of the outer disk by X-rays back-scattered by the extended ADC. Only a fully self-consistent treatment of the hydrodynamics and the radiation transfer can adequately handle the interdependence between the coronal structure and the radiation physics. We

have addressed this need by constructing a radiative-hydrodynamical algorithm to simulate such an environment in three-dimensional spherical space. The calculation reported here, which however assumes azimuthal symmetry, provides us with the spacetime profiles of density $\rho(r,\theta,t)$, velocity $\mathbf{v}(r,\theta,t)$, and the radiation energy density $u_r(r,\theta,t)$ of an accretion disk corona in a steady, luminous X-ray source radiating at half the Eddington limit. The results of simulations for other emission geometries and time-dependent sources will be discussed elsewhere. Our goal here is to present the details of the calculation first addressed by MZF, giving particular attention to the radiative aspects of the ADC. The coronal model and method of solution are described in §§ 2 and 3, respectively. §4 contains a full discussion of the results, and we give our conclusions in §5.

2. The Model

The model assumes that X-rays from the central source ionize and heat the disk's surface layers, inducing an evaporative flow that feeds the overlying corona. The details of this process have been discussed elsewhere (MZF). Here, we summarize the key points. The transition from a cool disk, where the gas temperature is set by a balance between atomic heating and cooling processes (primarily H I and He I; McCray and Hatchett 1975), and the hot corona whose temperature T_C is determined by the balance between Compton heating and inverse Compton cooling, occurs at a critical value Ξ_0 of the parameter $\Xi(J) \equiv 4\pi J/p_g$, where J is the local mean intensity of the radiation integrated over frequency, and p_g is the gas pressure. The actual value of Ξ_0 depends on the ionization state of the plasma, which itself depends on the flux of ionizing ultraviolet radiation. Previous studies have

found that Ξ_0 lies in the relatively narrow range $1-10$ for a large variety of power-law (Krolik, McKee, and Tarter 1981) and bremsstrahlung-like spectra (London, McCray, and Auer 1981). Since the X-ray spectra from binary X-ray sources are Planck-like, they are relatively deficient in ultraviolet radiation, and thus we assume $\Xi_0 = 10$ for our simulations.

Near the disk, the inverse Compton temperature is calculated as

$$T_{C0} = \frac{J_d T_d + J_r T_r}{J_d + J_r}, \tag{1}$$

where $J_d = (3/16\pi^2)(GM\dot{M}/R^3)$ and $T_d = (2\pi J_d/\sigma)^{1/4}$ are the mean intensity and temperature, respectively, of the radiation from the disk, and $J_r = cu_r/4\pi$ and $T_r = (L/4\pi\sigma R_*^2)^{1/4}$ are the mean intensity and temperature of the radiation from the central compact object. G is the gravitational constant, M is the stellar mass, σ is the Stefan-Boltzmann constant, and $\dot{M} = 2R_* L/GM$ is the mass accretion rate at the stellar surface. With the additional assumption of a planar flow at the disk boundary, one obtains the jump conditions from the conservation of energy and momentum, yielding an outflow velocity

$$v_0 = (2cR_g\,\Xi_0\,T_{C0}/\mu)^{1/3}, \tag{2}$$

where c is the speed of light, R_g is the gas constant, and μ is the mean molecular weight per free particle. With $\Xi_0 = 10$, $T_{C0} = 10^7$ K, and $\mu = 0.61$, $v_0 \approx 1 \times 10^9$ cm s^{-1}.

This outflow velocity depends only weakly on the flux and, by extension, the cylindrical radius. As such, the dynamically interesting region of the corona centers about the radius where v_0 equals the local escape velocity set by the effective gravitational acceleration (including radiative effects). Since the disk plasma possesses a Keplerian azimuthal velocity, this radius is $\sqrt{GM/v_0^2} \approx 2 \times 10^8$ cm. The domain of solution is selected to cover

a region that includes this radius. Assuming symmetry with respect to the disk axis and mirror symmetry with respect to the disk plane, we therefore confine the simulation region to the upper right hand quarter plane of (r, θ)-space, with the inner radial boundary at 1×10^7 cm, the outer radial boundary at 5×10^8 cm, and the disk surface boundary at $\theta = 87$ degrees.

This domain of solution is sufficiently close to the central X-ray source that a typical electron in the plasma undergoes many Thomson scatterings with the photons, with a mean free path $\langle l_e \rangle \approx 1/n_\gamma \sigma_T$, where n_γ is the photon number density and σ_T is the Thomson cross section. For a luminosity $L = 0.5\ L_{ed}$, the photon number density is $n_\gamma \sim \delta L/(4\pi c \langle \epsilon \rangle r^2)$, where $\langle \epsilon \rangle$ is the mean photon energy, and δ is a factor (generally less than one) accounting for shadowing by the corona. With $\langle \epsilon \rangle \approx 3$ keV and $\delta \approx 0.1$, the mean free path is evidently $\approx 3 \times 10^5\ (r/10^8 \mathrm{cm})^2$ cm. Thus, within the domain of solution, the plasma is strongly coupled to the radiation, and the sound speed depends on the total pressure, including radiation.

A second consequence of this strong coupling between the matter and the radiation is that the evaporated plasma quickly equilibrates to the inverse Compton temperature and is maintained at that temperature. The time scale for equilibration, $\tau_{eq} \equiv (3/8)(\mu_e/\mu)(m_e c^2/\delta L)(4\pi r^2/\sigma_T)$, where μ_e is the mean molecular weight per free electron, and m_e is the electron mass, is much smaller ($\sim 0.01/[r/10^8\ \mathrm{cm}]^2$ s) than the the flow time scale $\tau_f \equiv r/v_0 \approx 0.1\ [r/10^8\ \mathrm{cm}]$ s. The flow in the domain of solution is therefore nearly isothermal, with an equilibrium temperature

$$T_C = \frac{3.8}{4.0}\left(\frac{L}{4\pi\sigma R_*^2}\right), \tag{3}$$

which gives $T_C \approx 1.9 \times 10^7$ K for a neutron star with radius $R_* = 10$ km.

This situation greatly simplifies the set of equations needed for the simulation, since only the mass density ρ and the flow velocity $\mathbf{v}$ are unknown. We use the conservation of mass,

$$\frac{\partial \rho}{\partial t} + \nabla \cdot (\rho \mathbf{v}) = 0, \tag{4}$$

the conservation of momentum,

$$\rho\left[\frac{\partial \mathbf{v}}{\partial t} + (\mathbf{v} \cdot \nabla)\mathbf{v}\right] = -\nabla p_g - \rho \nabla \phi_g + \frac{\rho \kappa_T}{c}\mathbf{F}_f, \tag{5}$$

and the conservation of angular momentum,

$$\frac{\partial(\rho R v_\phi)}{\partial t} + \nabla \cdot (\rho R v_\phi \mathbf{v}) = 0, \tag{6}$$

to solve for ρ, the poloidal velocity $\mathbf{v_p}$, and the azimuthal velocity v_ϕ, respectively. Here, $p_g = \rho R_g T_C/\mu$ is the gas pressure, $\phi_g = -GM/r$ is the gravitational potential, κ_T is the Thomson scattering opacity, $\mathbf{F}_f$ is the radiation flux in the inertial frame of the flow, and R is the cylindrical radius.

Determining the radiation transport is nigh impossible if one does not make some approximation, even in the relatively simple case of Thomson scattering. The most general equation of radiative transfer is an integro-differential equation for the intensity. That is, the intensity at a given point and in a given direction depends on the intensity at every other point and in all directions. In order to simplify the equations governing the transport of radiative energy into simple partial differential equations, we apply the flux-limited diffusion theory developed by Levermore and Pomraning to the case of Thomson

scattering only (Melia and Zylstra 1991, MZ). In this case, we solve only the first angular moment equation

$$\frac{\partial u_r}{\partial t} + \nabla \cdot \mathbf{F} = -\rho \kappa_T \mathbf{F} \cdot \beta \tag{7}$$

for the radiation energy density u_r. The radiation flux $\mathbf{F}$ is then given by equation (29) of MZ, with a dependence only on the local values of the mass density, the flow velocity, and the radiation energy density and its first order spatial derivative.

At the disk boundary, the polar angular velocity is kept constant at a value of $-v_0$, where v_0 is given by equation (2), though the radial velocity component decreases linearly to zero below this transition plane. The azimuthal velocity is set to the (constant) Keplerian value $\sqrt{GM/r}$. In addition, the mass density is here set at a value linearly dependent on the impinging flux: $\rho_0 = \mu F_i / c R_g \, \Xi_0 \, T_{C0}$, where $F_i = \mathbf{n}_d \cdot \mathbf{F}$ and $\mathbf{n}_d$ is the outward normal to the disk's surface, specified by the height-radius relation $h(R) = 1\,(R/10^7\ \mathrm{cm})^{1.1}$ km.

Except for the azimuthal velocity, the hydrodynamic variables are constant at the inner radial boundary, set at the values found just above the boundary. The azimuthal velocity scales as $1/r$ in order to conserve the specific angular momentum, and the radiation energy density is fixed at its free streaming value.

At the outer radial boundary, all of the hydrodynamic variables are constant, set at the values found just below the boundary. Here, the radiation energy density scales as $1/r^2$ and the radiation diffusion coefficient is modified such that the diffusive flux equals $c\,u_r$. We employ reflective boundary conditions at the polar axis.

3. Method of Solution

The two-dimensional structure (using spherical coordinates $[r, \theta]$) of the accretion disk corona is determined numerically on an Eulerian grid of (70 radial $\times$ 60 polar) cells covering the domain of solution. The size of the cells is chosen to reflect the required resolution, with the smaller dimensions corresponding to the inner radial boundary and the disk surface.

Our radiative-hydrodynamical scheme is based on the piecewise parabolic method (PPM) of Colella & Woodward (1984), though with the addition of radiation transport, whose implementation includes the effects of radiation pressure in the Riemann solver, the radiative force in the momentum equation, and the exchange of internal energy resulting from the interaction between the matter and radiation. With the known values of the hydrodynamic variables and the explicit evaluation of the FDT coefficients from the most recent determination of the radiation energy density u_r, the finite difference version of the transport equation is simply a combination of linear algebraic expressions for the updated value of u_r. Using the operator-split method described below (in which u_r is obtained for one row of cells at a time), this set of relations reduces to a tridiagonal system of equations that is readily solvable. It is straightforward to obtain the FDT coefficients in each cell from the root $A = 1 - 2\vec{f} \cdot \vec{\beta}$ to the set of equations in MZ that determine the normalized flux $\vec{f}$ (eq. 26 of MZ), using a hybrid of the Newton-Raphson and bisection methods.

The operator-split method employed by our radiative-hydrodynamical code determines the density, flow velocity, and radiation energy density in one row of cells at a time. At a given time step, the code sweeps through the radial and then the polar grid rows,

accounting only for the fluxes and the component of the vector quantities in the direction of the sweep. Of course, all the components of the radiation vector $\vec{L}$ are included in the evaluation of its magnitude. Figure 1 is a schematic diagram showing this two-time-step sequence, along with a specification of the time interval. With our implicit calculation of the radiative transfer (see above), the time step itself is restricted primarily by the Courant condition (for which we assume a factor of 0.8). However, to prevent the flow from attaining unphysically large sound speeds (and thus exceedingly small time steps) in regions of very low density, we assume a minimum mass density of 2×10^{-9} g cm^{-3} throughout the domain of interest. This value is sufficiently small to be dynamically unimportant. In addition, we impose the restriction that no mass may leak out from cells at this minimum density in order to avoid the local "creation" of matter in these regions. We note that the implicitness of this method for handling the radiation transfer is reflected not only in having the new value of u_r in each cell depend on the new values of the neighboring cells, but also in using the most recent values of u_r in neighboring cells perpendicular to the sweep direction for the evaluation of the FDT coefficients. As shown in this figure, the sweep directions for both the hydrodynamic and radiative determinations are alternated with each successive time step.

To calculate the angle- and time-dependent flux seen by a distant observer, we integrate over the intensity from the visible emitting area (see Figure 2 for a definition of the relevant geometrical parameters). In this scheme, the emission surface is assumed to be a sphere located at $\vec{r}_{out}$ near the outer radial boundary of the domain of solution. The observer is positioned at $\vec{D}$, making an inclination angle i with respect to the symmetry

axis $\hat{z}$. The observed flux is then given by the integral

$$F(\vec{D}) = \int_{-1}^{1} d\mu \int_{0}^{2\pi} d\phi \, I(\vec{r}_{out}, \hat{n}) \, \frac{r_{out}^2}{|\vec{D} - \vec{r}_{out}|^2} \, \frac{\hat{n} \cdot \vec{D}}{|\vec{D}|}, \tag{8}$$

where μ ($\equiv \cos\theta$) and ϕ are the angular coordinates on the emitting sphere and $\hat{n} \equiv (\vec{D} - \vec{r}_{out})/|\vec{D} - \vec{r}_{out}|$ is the unit vector pointing in the direction toward the observer.

In FDT, the intensity I is given as

$$I(\vec{r}_{out}, \hat{n}) = c\, u_r(\vec{r}_{out})\, \psi(\vec{r}_{out}, \hat{n}), \tag{9}$$

where ψ is the normalized intensity given by equation (9) of MZ. However, due to our limited grid resolution (see above), ψ is known only at the coordinates (r_{out}, θ_j), with $j = 1, \ldots, 60$. In addition, the intensity profile (as a function of angle) can be extremely narrow, particularly in regions of very low density, where the radiation is streaming freely. It is therefore necessary to interpolate the evaluated intensity distributions at the grid points to obtain a continuous profile at all intervening points. In practical terms, this procedure constitutes the evaluation of the intensity maxima I_{max} and their directions $\hat{n}_{max}$ at the grid points, and a set of cone angles $\{\vartheta_n\}$ relative to I_{max} that corresponded to the maximum angles within which the intensity exceeds specified fractions of I_{max}. In our calculations, we use a set of five cones ($n = 1, \ldots, 5$) with corresponding intensity fractions of 0.8, 0.4, 0.1, 0.01, and 0.0001. With this information, the visible portion of the emitting surface may be divided into areas in which the observer is either within or outside of these cones. Then, for a polar angle $\theta_{j-1} \leq \theta \leq \theta_j$, the interpolated direction of maximum intensity is given as

$$\hat{n}_{max}(\theta) = \hat{n}_{max}(\theta_{j-1}) + \frac{\theta - \theta_{j-1}}{\theta_j - \theta j - 1}[\hat{n}_{max}(\theta_j) - \hat{n}_{max}(\theta_{j-1})], \tag{10}$$

with the corresponding cone angle,

$$\vartheta_n(\theta) = \vartheta_n(\theta_{j-1}) + \frac{\theta - \theta_{j-1}}{\theta_j - \theta_{j-1}}[\vartheta_n(\theta_j) - \vartheta_n(\theta_{j-1})] \,. \tag{11}$$

Between each pair of neighboring grid polar angles, the area's boundary values of θ and ϕ are given by the minimum and maximum boundary values found in stepping through these grid polar angles. Thus, between two neighboring grid polar angles, an area of given intensity fraction is a simple rectangle in (θ, ϕ)-space. The visible emitting surface between two neighboring grid polar angles is further divided into sub-areas whose boundary values of polar angle and azimuth consist of the boundary values of polar angle and azimuth of the area of the intensity fraction of interest and those of the area of the next largest intensity fraction. Figure 3 shows schematically all the possible divisions into subareas of the area of a given intensity fraction between neighboring grid polar angles. The solid and dashed lines denote the areal and sub-areal boundaries, respectively. The hatched area corresponds to the area of the next largest intensity fraction. If the area of interest shares with the area of next largest intensity fraction three common boundary values of polar angle or azimuth, then only one subarea covers the region consisting of the area of interest excluding the area of the next largest intensity fraction. If the two areas have the same boundary values of the polar angle or of the azimuth, then two subareas cover the non-excluded region. If the two areas share one boundary value in polar angle and one boundary value in azimuth, then three subareas cover the non-excluded region. If an area of larger intensity fraction does not exist within the area of interest, then four equal subareas cover this area. If the two areas share only one boundary value of polar angle or azimuth, then five subareas cover the non-excluded region. Finally, if the areas do not

share any common boundary values, then eight subareas cover the non-excluded region.

We impose a 10×10 grid of cells over each sub-area, within which the polar angular and azimuthal extent is assumed to be constant. We then sum the integrand of equation (1) evaluated at each cell over the visible emitting surface and obtain the radiative flux seen by the observer. To evaluate the observed intensity at a cell located at (θ, ϕ), where $\theta_{j-1} \leq \theta \leq \theta_j$, we interpolate linearly with respect to θ the intensities sampled from the profiles at the neighboring grid polar angles, θ_{j-1} and θ_j, after rotating each profile such that their maximum intensities point in the direction of the local maxima given by equation (3). More specifically, the intensity on the emitting surface at (θ, ϕ) is

$$I(\theta, \phi; \hat{n}) = I(\theta_{j-1}, \phi; \hat{n}_l) + \frac{\theta - \theta_{j-1}}{\theta_j - \theta_{j-1}}[I(\theta_j, \phi; \hat{n}_r) - I(\theta_{j-1}, \phi; \hat{n}_l)], \tag{12}$$

where $\hat{n}$ is the direction from the source to the observer at the point of interest, and

$$\hat{n}_l = \hat{n} - \hat{n}_{max} + \hat{n}_{max,l}, \tag{13}$$

$$\hat{n}_r = \hat{n} - \hat{n}_{max} + \hat{n}_{max,r} \tag{14}$$

and where $\hat{n}_{max,l}$ and $\hat{n}_{max,r}$ are the directions of maximum intensity at the $(j-1)^{th}$ and j^{th} grid polar angles, respectively, on the emitting surface.

4. Results

The simulation presented here assumes the following initial conditions: (1) the corona is at (uniform) minimum density (2×10^{-9} g cm^{-3}), (2) the poloidal velocity is zero everywhere, and (3) the azimuthal velocity is

$$v_\phi = \sqrt{\frac{GM}{r}} \sin\theta, \tag{15}$$

which balances the centripetal force due to gravity in the cylindrical radial direction. The radiation energy density is initially set equal to its free-streaming value for a luminosity of 0.50 times the Eddington limit ($L_{ed} = 1.04 \times 10^{38}$ ergs s^{-1} for a 1.4 $M_\odot$ neutron star). During the simulation, the radiation flux at the inner radial boundary, r_i, is independent of polar angle and is maintained at a level of $0.50\, L_{ed}/(4\pi r_i^2)$. In addition, the radiation temperature is taken to be that of the stellar surface (with radius $R_* = 10^6$ cm) emitting as a black body, i.e., 1.96×10^7 K for this particular luminosity. The gas temperature is set at a value 3.8/4.0 times smaller, or $\approx 1.86 \times 10^7$ K. This simulation proceeds for approximately 1.7 seconds, during which time matter evaporates from the disk surface with a velocity of $\sim 1 \times 10^9$ cm s^{-1} and a density that depends linearly on the impinging flux. The calculation ends when the time-averaged evaporation mass rate has equaled the wind mass loss rate for $\sim$1 second (see Figure 2 of MZF).

As noted earlier (MZF), the accretion disk corona is comprised of two main regions: (1) an inner, highly dynamic portion, whose vertical structure varies quasi-periodically on a dynamical time scale, and (2) an outer, more stable zone in which the evaporated plasma rises to form a sheath that gradually merges into a wind at large radii. The critical radius r_{crit} that divides these two regions is the radius where the outflow velocity of the evaporated plasma at the disk surface equals its escape velocity, which is determined in part by the location along the disk at which the ram pressure $\rho_0 v_0^2$ of the evaporated gas dominates over the external pressure due to the incident radiation.

In the inner corona, gravity and radiation significantly retard the vertical motion of the evaporated flow and a sheath forms with the ram-pressure support of the ionized

gas from the disk below. Since the plasma cannot escape from the inner corona, this sheath becomes more massive and optically thick, and the gravitational force and radiation pressure across it correspondingly increase. However, during this process, the supporting ram pressure decreases in strength because of the increased shadowing by the corona, and so the structure is forced to collapse back down onto the disk, where the process begins anew. The resulting profile is dynamic and "bubbly", with quasi-periodic oscillations on a dynamical time scale.

In contrast, the flow within the outer corona is relatively stable. Here, the evaporated plasma rises vertically until it reaches a relatively dense sheath projecting outward with an angle of roughly 40 degrees with respect to the disk's surface, and eventually forms a wind at large radii. This mass outflux is relatively steady because the influence of gravity and radiation pressure gradients are balanced by the coronal ram pressure support.

The details of this dynamical structure are displayed in Figures 4, 5, and 6. The six panels of Figure 4 show the coronal evolution between the simulation times 1.2 and 1.7 seconds, in steps of 0.1 seconds. The velocity field at the end of this sequence is represented by the poloidal vectors in Figure 5 and the azimuthal velocity contours in Figure 6. In Figure 4, the iso-density contours correspond to mass density values of 5×10^{-5} g cm^{-3} times 0.5^n, where $n = 0, 1, \ldots, 14$. The two-part structure is quite evident, with $r_{crit} \approx 1.5 \times 10^8$ cm. Within the inner corona, the bubbly structure rises and falls quasi-periodically every $\sim 0.2 - 0.3$ seconds, which is roughly the dynamical time scale at the critical radius, i.e., $\tau_{dyn}(r_{crit}) \equiv \sqrt{r_{crit}^3/GM} \approx 0.1$ seconds. The constancy of the mass density distribution between the disk and the sheath in the outer corona indicates

that the flux impinging on the outer disk surface is relatively constant, which itself suggests that this flux is largely due to scattering off the stable (outer) sheath.

Not surprisingly, the larger evaporative flux and stronger gravitational acceleration at smaller radii induce higher mass densities ($\sim 3 \times 10^{-5}$ g cm^{-3}) in the inner corona relative to those ($\sim 3 \times 10^{-6}$ g cm^{-3}) in the outer structure. The sheath in the inner corona is clumpy with density enhancements as large as an order of magnitude. In contrast, the sheath in the outer corona is stratified, though there is some clumpiness near the disk. Within the sheath itself, the density increases by a factor of $30 - 60$, with the smaller gradients at progressively larger radii.

In Figure 5, panel (a) shows the poloidal velocity field within the inner corona at spherical radii $r \leq 2 \times 10^8$ cm, whereas panel (b) shows the analogous field in the outer corona for spherical radii $r \geq 2 \times 10^8$ cm. The length of the arrows corresponds to the magnitude of the velocity on a $\log_{10}$ scale, starting from 1×10^7 cm s^{-1} and extending up to 1×10^{10} cm s^{-1} (see the standard arrow shown in the upper left hand corner of each panel). At this simulation time (i.e., 1.7 seconds), the inner coronal sheath is collapsing back down onto the disk. Between the disk and sheath in the outer corona, the evaporated plasma rises nearly vertically with a velocity of $\sim 1 \times 10^9$ cm s^{-1}. At large radii there is a slight outward radial displacement due to the centrifugal force induced by the plasma's azimuthal motion, and the flow is diverted outward along the sheath by gas pressure, where it blends into a wind with a velocity of $\sim 3 \times 10^8$ cm s^{-1} and a mass loss rate of $\approx 1 \times 10^{19}$ g s^{-1}. As dicussed by MZF, this is about 10 times greater than the mass accretion rate through the disk at the stellar surface (see Figure 2 of MZF).

The distribution of azimuthal velocity within the outer corona is shown in Figure 6, together with contours (represented by the thick curves) of values for which the induced centrifugal force is balanced by the cylindrical radial component of gravity. Since the evaporated plasma leaves the disk with the (local) Keplerian value of v_ϕ and it experiences zero torque, its azimuthal velocity initially stays nearly constant at a value $\sim 1/\sqrt{R}$. At the sheath, however, v_ϕ decreases sharply due to the merging of the evaporated plasma with gas advected outward along this density enhancement. As a result, v_ϕ eventually drops of as $1/R$, significantly faster than the azimuthal velocity of the vertical flow above the disk. Thus, the centrifugal force on the sheath is weak compared with gravity.

Since the flow in the corona is isothermal, the density contours in Figure 4 also represent the isobaric regions. We can thus determine from this Figure the direction of the force due to gas pressure and its strength relative to gravity. This force acts in a direction perpendicular to the iso-density curves toward the region of smaller gas pressure, with a strength relative to gravity given by

$$\frac{|\nabla p_g|}{|\rho \nabla \phi_g|} = |\nabla(\ln \rho)| \frac{R_g T}{GM\mu} r^2 \approx 1.34 \times 10^{-11}\,\mathrm{cm}^{-1}\,|\nabla(\ln \rho)|\, r^2. \tag{16}$$

For example, at a radius of 3.5×10^8 cm, the value of $|\nabla \ln \rho|$ within the sheath is $\sim 2 \times 10^{-8}$ cm^{-1}, so that the force along the sheath due to gas pressure is only $\approx 3\%$ of that due to gravity. The relative magnitude above the disk is similar, and so we conclude that the gas pressure in these regions is ineffective, which is not surprising given that the flow here is supersonic. This is not the case everywhere, however, since the radiative force on the coronal plasma must be balanced by an appropriately large gas pressure gradient across the sheath. In fact, the magnitude of $\nabla(\ln \rho)$ in this direction is $\sim 2 \times 10^{-2}$ cm^{-1}, which

represents a force ratio of about 5. It is primarily this feature of the density structure that diverts the flow into an outwardly-directed wind.

One reason for the difference between the coronal structure described here and that of earlier models (e.g., Begelman, McKee, and Shields 1983) may be traced to the latter's assumption of hydrostatic equilibrium in the vertical direction, which leads to a gaussian density profile. It is apparent that when dynamic effects are included, the instantaneous vertical mass distribution is in fact non-gaussian. Nonetheless, it is useful to gauge how closely a time-averaged structure can mimic a hydrostatic profile. The panels in Figure 7 compare the actual density distributions averaged over the last 0.8 seconds of the simulation (solid curves) with appropriately normalized gaussian fits (dashed curves), at cylindrical radii $R = 1.5 \times 10^7$, 2.9×10^7, 5.5×10^7, and 1.0×10^8 cm. These gaussian fits have the same column density and either the same maximum density or base density as the actual time-averaged profile (see Table 1). It is apparent that the time-averaged profiles can be gaussian-like, though with two very important differences: (1) there is a significant deficit in density at the upper end due to the pressuring effect of the impinging radiation, and (2) there is no global gaussian function that describes the profile at all radii, i.e., the fit is necessarily local and the parameters change with radius.

Let us next consider the effects of this coronal structure on the radiation field. The contours of radiative energy density u_r at the simulation time 1.7 seconds are displayed in Figure 8, which shows that the distribution is near free streaming along the polar axis, but is smaller below the sheath due to coronal shadowing effects. It is a simple matter to ascertain from these iso-density contours the direction of the total radiation flux $\vec{F}$,

which points in a direction perpendicular to the surfaces of constant u_r toward regions of lower density. Not surprisingly, $\vec{F}$ is radial along the polar axis. However, the flux points in a slightly poleward direction above the sheath, indicating that the radiation field is partially reflected off this mass density enhancement. Within the sheath, $\vec{F}$ generally points radially outwards, though with a diskward slant in the lower layers. The direction of $\vec{F}$ above the disk suggests that most of the impinging flux is in fact scattered into the disk by the overlying coronal sheath.

This behavior of the radiation field is brought out explicitly by the curves in Figure 9, which correspond to the magnitude (heavy line) of the flux normalized by the persistent (0.5 Eddington) value and the angle η made by the flux vector with respect to the radial direction, with η increasing diskward. Evidence for a strong reflection of the X-rays by the sheath is provided by an enhancement of $\approx 40\%$ in F/F_0 and a negative value of η (≈ -5 degrees near an inclination of 55 degrees). The flux decreases by almost two orders of magnitude within the sheath, and points progressively diskward with increasing inclination angle. Below the sheath, F increases slightly and points in a more radial direction due to contributions from neighboring lower parts of the corona.

Finally let us consider the effect of the accretion disk corona on the flux seen by a distant observer. In Figure 10, we show the intensity as a function of the poloidal angle for three grid points straddling the outer sheath. These curves give perhaps the clearest indication of the usefulness of our flux-limited diffusion theory as implemented in the radiative-hydrodynamic algorithm used for this simulation. Just above the sheath, the intensity profile is narrow with its maximum offset poleward from the radial direction

by $\approx$ 4 degrees. In fact, the intensity in the radial direction here is ~ 100 times lower than the maximum intensity. Deep within the sheath, the profile is very broad due to the significant degree of scattering in this region. But the intensity profile narrows again below the sheath, this time showing a maximum toward the disk, confirming the behavior of the flux discussed above.

These features of the radiation field translate directly into the observational characteristics of the flux seen by a distant observer (Figure 11). At inclination angles $i \leq 48$ degrees, F can be as much as twice the flux emitted directly by the neutron star, whereas it decreases to a tenth of this value deep in the shadow of the corona. Therefore, the partial (poleward) reflection of X-rays by the upper corona can greatly enhance the flux observed at low inclination angles, whereas attenuation of the direct X-ray flux greatly suppresses the observable flux close to the disk's surface.

5. Conclusions

We have found that the accretion disk corona consists of two main regions: (1) a highly dynamic, inner zone in which the vertical structure oscillates quasi-periodically on a dynamical time scale, and (2) a relatively stable outer portion in which the evaporated disk plasma rises vertically from the disk surface, deflects along an enveloping dense sheath forming a wind at larger radii. The critical radius that marks the transition from one segment to the next is given roughly by the location at the disk surface where the outflow velocity equals the escape velocity determined by the local, effective gravitational field (which includes the influence of the impinging radiation). Within the outer corona, the evaporative mass loss rate can be as much as 10 times greater than the mass accretion rate through the disk (see MZF for addition discussion on this feature).

With a density inversion supported by ram pressure, the instantaneous ADC structure differs significantly from the gaussian hydrostatic profile assumed by earlier models (e.g., Begelman, McKee & Shields 1983). Even though the time-averaged vertical density in the inner corona locally approximates a gaussian very close to the disk, it differs from a gaussian at larger values of z due to a deficit in mass, and it differs globally from the gaussian distribution expected from earlier models in the variation of scale height with radius.

A significant fraction of the photons emitted from the central X-ray source are reflected polewards by the corona. As a result the flux seen by a distant observer is strongly affected by the ADC. This scattering enhances the observed flux by as much as 100% for observers

in direct sight of the central X-ray source, but suppresses the flux by an order of magnitude for observers deep in the coronal shadow.

As alluded to by MZF, the large mass loss rates in the wind and inner corona raise important issues regarding the accretion disk structure and the evolution of the binary (see also Melia & Lamb 1987; Lamb & Melia 1987), since estimates of the driving torques based on an accretion rate inferred from L can severly underestimate tha actual mass transfer rate from the companion. Including the effect of the corona on the observed flux therefore implies that X-ray bright binary systems may be evolving 5 to 100 times faster (the factor by which $\dot{M}$ at the outer edge of the disk exceeds the apparent rate) than is inferred from direct observations.

These questions will be addressed in our continuing study of ADCs in LMXRBs. Of particular interest is the response of the corona to a time-dependent X-ray flux at the central source. The ensuing burst-induced evaporative flow can significantly alter the observed light profile relative to that associated with the emissivity of the source itself (Melia 1987; Melia, Zylstra & Fryxell 1992; Melia & Zylstra 1992).

This research was supported in part by NSF grant PHY 88-57218, NASA grant NAGW-2380, and the Alfred P. Sloan Foundation. Most of the numerical calculations were carried out at the National Center for Supercomputing Applications in Urbana-Champaign.

References

Begelman, M.C., McKee, C.F., and Shields, G.A. 1983, *Ap. J.*, **271**, 70.

Colella, P. & Woodward, P.R. 1984, *J. Comp. Phys.*, **54**, 174.

Krolik, J.H., McKee, C.F., and Tarter, C.B. 1981, *Ap. J.*, **249**, 422.

Lamb, D.Q. & Melia, F. 1987, *Ap. J. (Letters)*, **321**, L133.

London, R.A., McCray, R., and Auer, L.H. 1981, *Ap. J.*, **243**, 970.

McClintock, J.E., London, R.A., Bond, H.E., and Grauer, A.D. 1982, *Ap. J.*, **258**, 245.

McCray, R., and Hatchett, S. 1975, *Ap. J.*, **199**, 196.

Melia, F. 1987, *Ap. J. (Letters)*, **315**, L43.

Melia, F. & Lamb, D.Q. 1987, *Ap. J. (Letters)*, **321**, L139.

Melia, F. & Zylstra, G.J. 1991, *Ap. J.*, **374**, 732. (MZ)

Melia, F. & Zylstra, G.J. 1992, *Ap. J. (Letters)*, submitted.

Melia, F., Zylstra, G.J., and Fryxell, B. 1991, *Ap. J. (Letters)*, **377**, L101. (MZF)

Melia, F., Zylstra, G.J., and Fryxell, B. 1992, *Ap. J. (Letters)*, in press.

White, N.E., and Holt, S.S. 1982, *Ap. J.*, **257**, 318.

White, N.E., Peacock, A., and Taylor, B.G. 1985, *Ap. J.*, **296**, 475.

TABLE 1

Parameters For The Gaussian Fits In Figure 7

Cylindrical Radius (cm)	Base Density (g cm^{-3})	Column Density (g cm^{-2})	Scale Height (cm)
1.5×10^7	2.00×10^{-5}	13.01	7.35×10^5
2.9×10^7	1.50×10^{-5}	32.85	2.46×10^6
5.5×10^7	2.56×10^{-6}	24.63	1.09×10^7
1.0×10^8	7.72×10^{-7}	22.77	3.32×10^7

Figure Captions

Figure 1. Schematic flow chart of the two-time-step sequence followed by the radiative-hydrodynamics algorithm.

Figure 2. The geometry used to determine the radiative flux seen by an observer at $\vec{D}$, making an inclination angle i with respect to the symmetry axis $\hat{z}$. The 'emitting' surface is a sphere of radius r_{out}, located near the outer radial boundary of our domain of solution. The angles θ and ϕ are position angles of an elemental area on this surface.

Figure 3. A schematic representation of the areal division corresponding to a given intensity fraction between two neighboring grid polar angles into sub-areas (labeled by number) as described in the text. The solid lines denote the boundaries of the areas of specified intensity fractions. They serve also as boundaries of the sub-areas, along with the dashed lines. The hatched area is an area of larger intensity fraction.

Figure 4. Contours of mass density in the accretion disk corona at (simulation) times (a) t = 1.2 s, (b) t = 1.3 s, (c) t = 1.4 s, (d) t = 1.5 s, (e) t = 1.6 s, and (f) t = 1.7 s. Iso-density curves correspond to values of 5×10^{-5} g cm$^{-3} \times 0.5^n$, where $n = 0, 1, \ldots, 14$. The contours in panel (a) are labelled by the appropriate values of n. The corona consists of two main parts: a dynamic, inner region with a bubbly density stucture, and a relatively stable, enveloping sheath in the outer zone.

Figure 5. Polodial velocity field within the (a) inner and (b) outer portions of the accretion disk corona at t = 1.7 s. The length of the arrows denotes the velocity magnitude on a $\log_{10}$

scale starting at 1×10^7 cm s^{-1} and extending to 1×10^{10} cm s^{-1} (see the standard arrow in the upper left hand corner of each panel). Plasma circulates between the inner disk and corona. The evaporated gas leaves the outer disk vertically with a velocity $\sim 1 \times 10^9$ cm s^{-1}, deflects off the sheath, and blends into an outwardly-directed wind with a velocity of $\sim 3 \times 10^8$ cm s^{-1}.

Figure 6. Contours of azimuthal velocity v_ϕ in the accretion disk corona at simulation time t = 1.7 seconds. The thin iso-density curves of v_ϕ correspond to values of 10^9 cm s^{-1} times 0.9^n, where $n = 0, 1, \ldots, 4$. The thick iso-density curves have the same values, but correspond to the locations where the induced centrifugal force balances the cylindrical radial component of gravity. The azimuthal velocity of the flow decreases rapidly when it enters the sheath due to the outward advection of plasma with smaller specific angular momentum.

Figure 7. Vertical density profiles (solid curves) in the inner corona averaged over the last 0.8 seconds of the simulation at cylindrical radii (a) 1.5×10^7 cm, (b) 2.9×10^7 cm, (c) 5.5×10^7cm, and (d) 1×10^8 cm. The dashed curves show the corresponding gaussian fits assuming the same column depth and either the same maximum density (plot a) or the same base density (plots b, c, and d). The column depths and density scale heights of these gaussian fits are given in Table 1.

Figure 8. Contours of radiation energy density in the accretion disk corona at simulation time t = 1.7 s. The iso-density curves correspond to values of 2×10^{12} ergs cm^{-3} times 0.5^n, where $n = 0, 1, \ldots, 15$. Strong shadowing effects by the corona are indicated in the outer regions, and the flux, which points in a direction perpendicular to these

contours, is scattered onto the outer disk by the ionized plasma within the sheath.

Figure 9. Local radiation flux F in the poloidal plane near the outer radial boundary normalized to the half-Eddington value F_0, and the angle η this flux makes with respect to the radial direction, as a function of polar angle θ. Scattering in the corona enhances the flux above the sheath by as much as 40% and suppresses it by up to a factor of ~ 30 near the disk surface.

Figure 10. Intensity in the poloidal plane near the outer radial boundary as a function of angle η (increasing diskward) with respect to the radial direction at time t = 1.7 s. The 3 panels correspond to the polar angles (a) $\theta = 48$ degrees (just above the sheath), (b) $\theta = 59$ degrees (within the sheath), and (c) $\theta = 73$ degrees (between sheath and disk). Thomson scattering strongly affects the radiation field within the corona. Just above the sheath, the intensity along the radial direction is ~ 100 times less than the maximum intensity shifted four degrees poleward of the radial direction. Significant scattering within the sheath broadens the profile. The profile between the sheath and disk indicates that practically all of the intensity there is scattered by the sheath.

Figure 11. Observed flux F (normalized to the half-Eddington value F_0) as a function of inclination angle i at t = 1.7 s. Thomson scattering within the accretion disk corona enhances by up to 100% the flux seen by a distant observer in direct view of the central X-ray source, and it suppresses the observable flux by an order of magnitude or more deep within the coronal shadow.

Figure 1

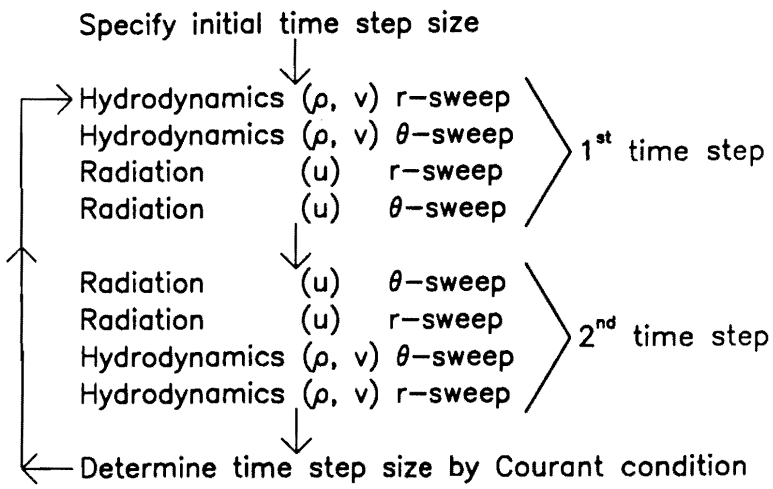

Figure 2

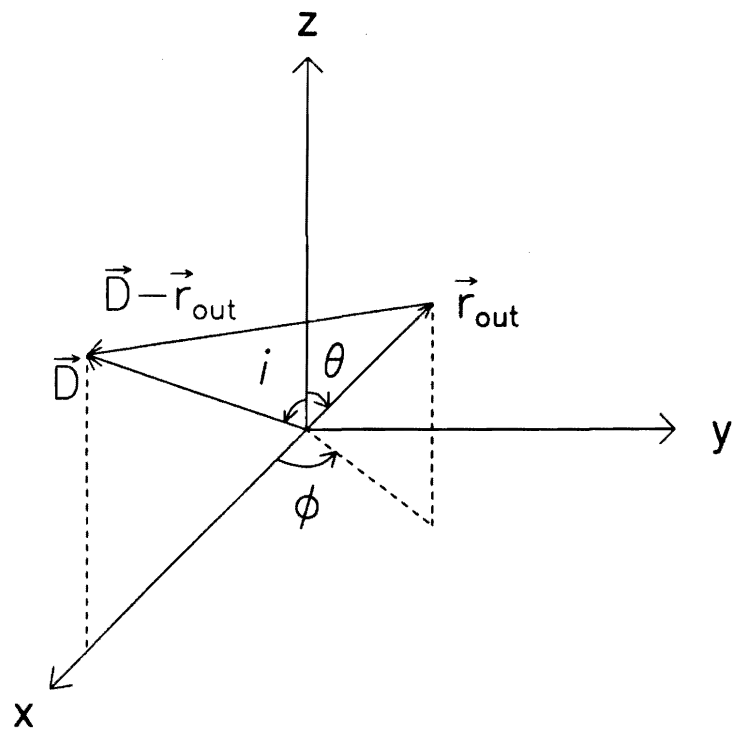

Figure 3

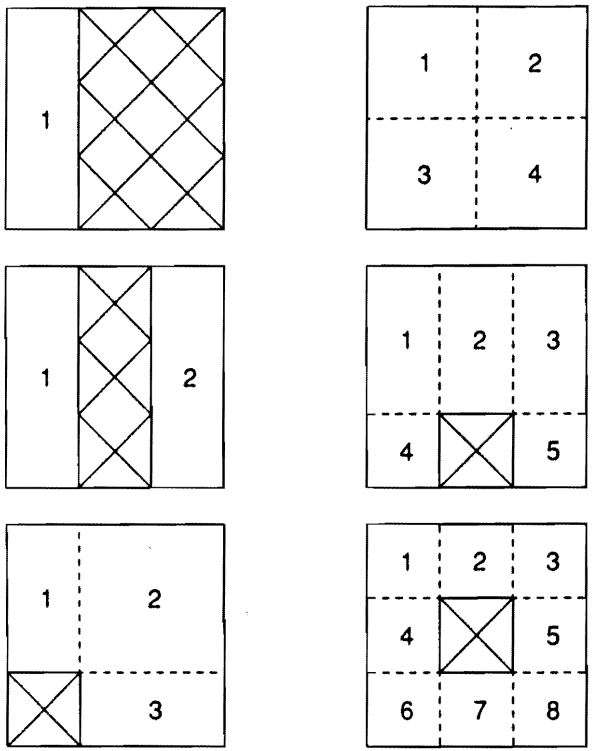

Figure 4(a)

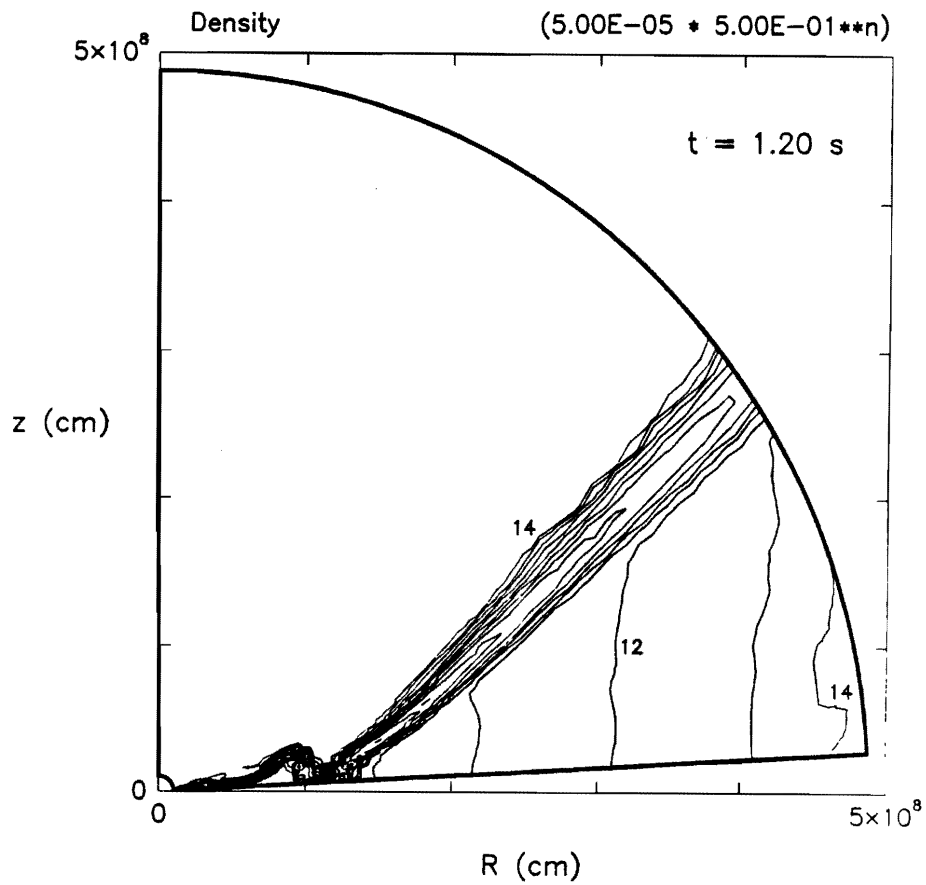

Figure 4(b)

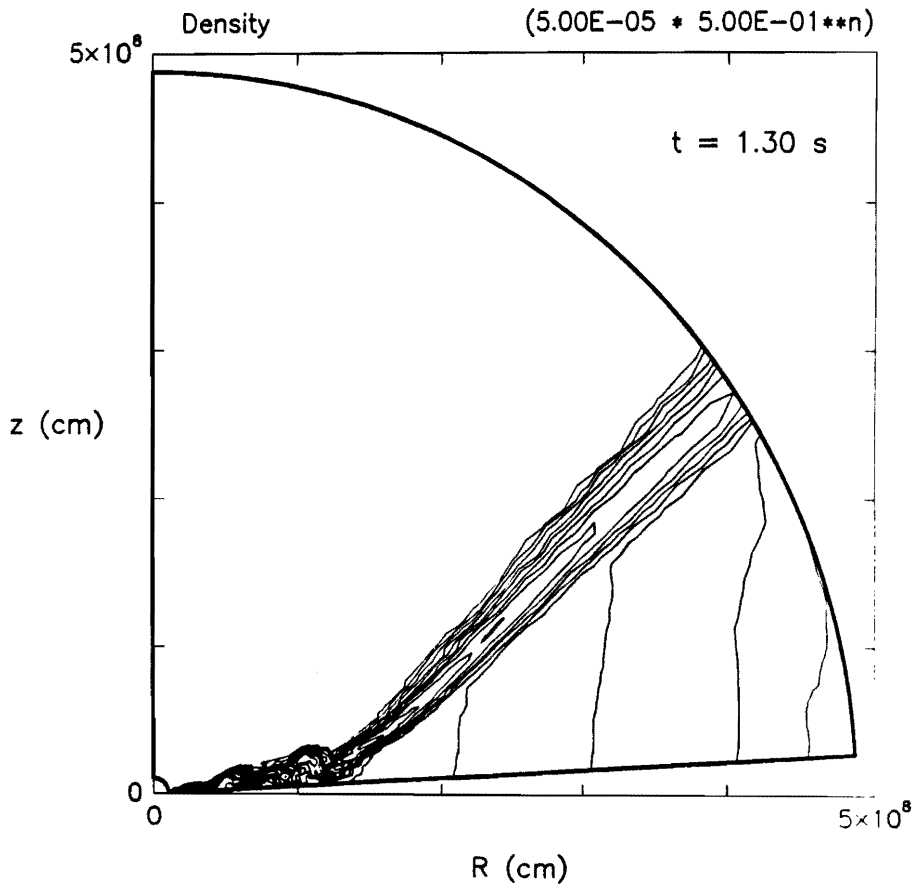

Figure 4(c)

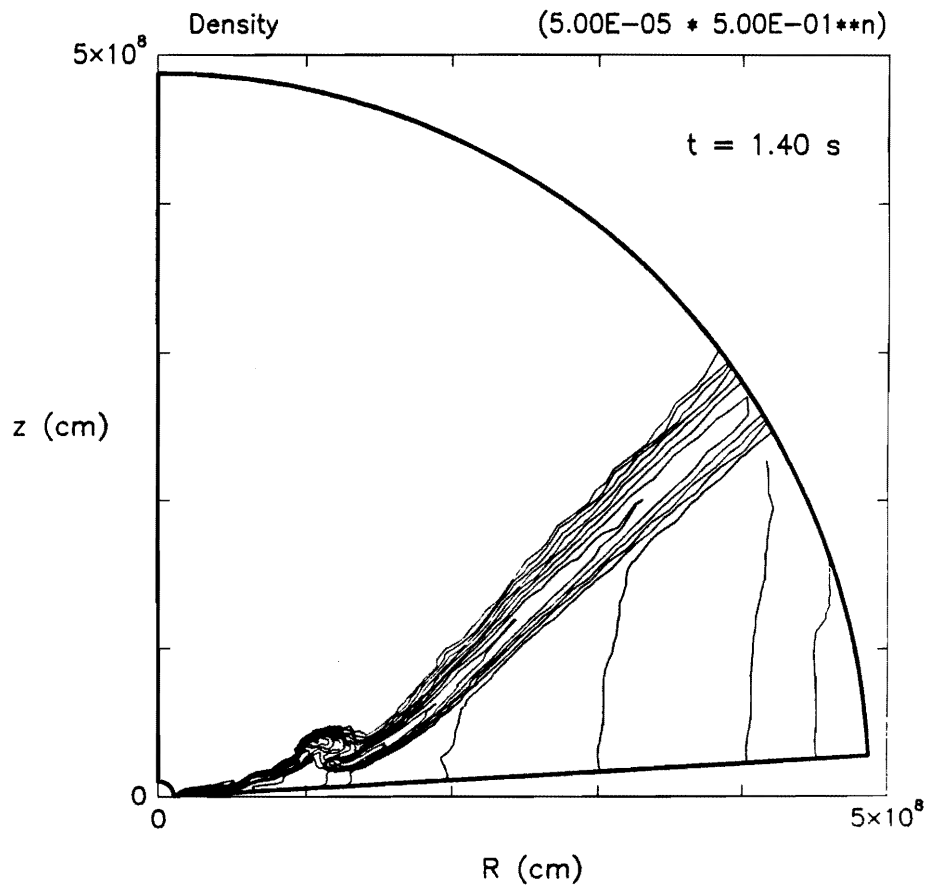

Figure 4(d)

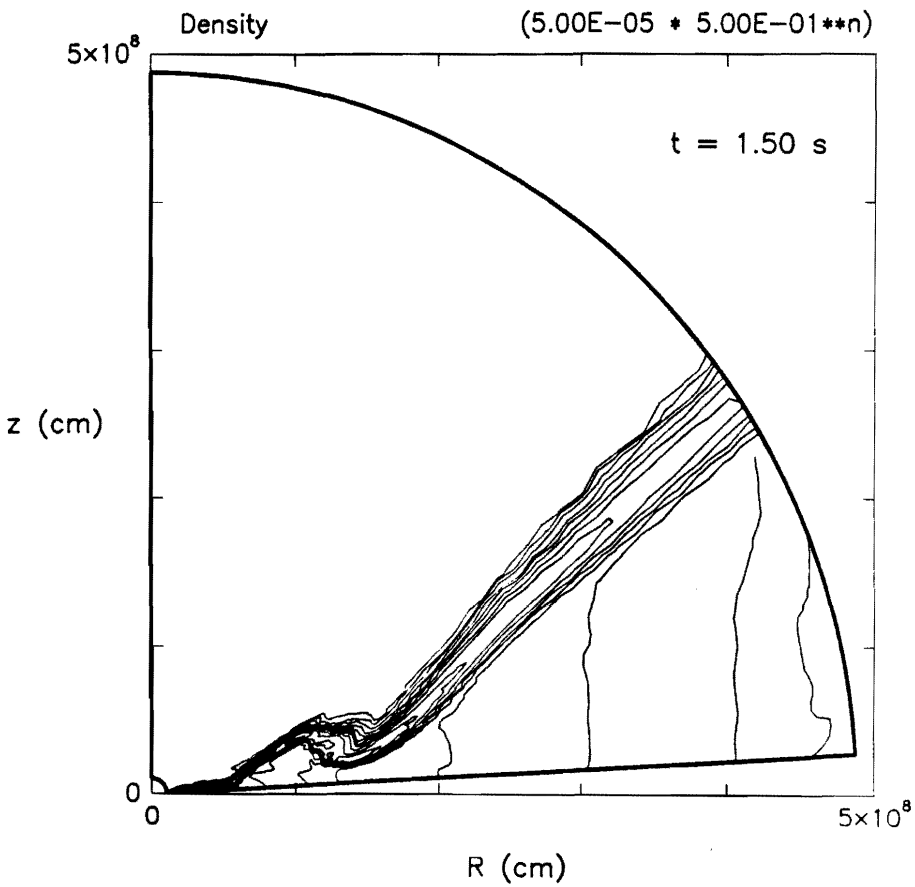

Figure 4(e)

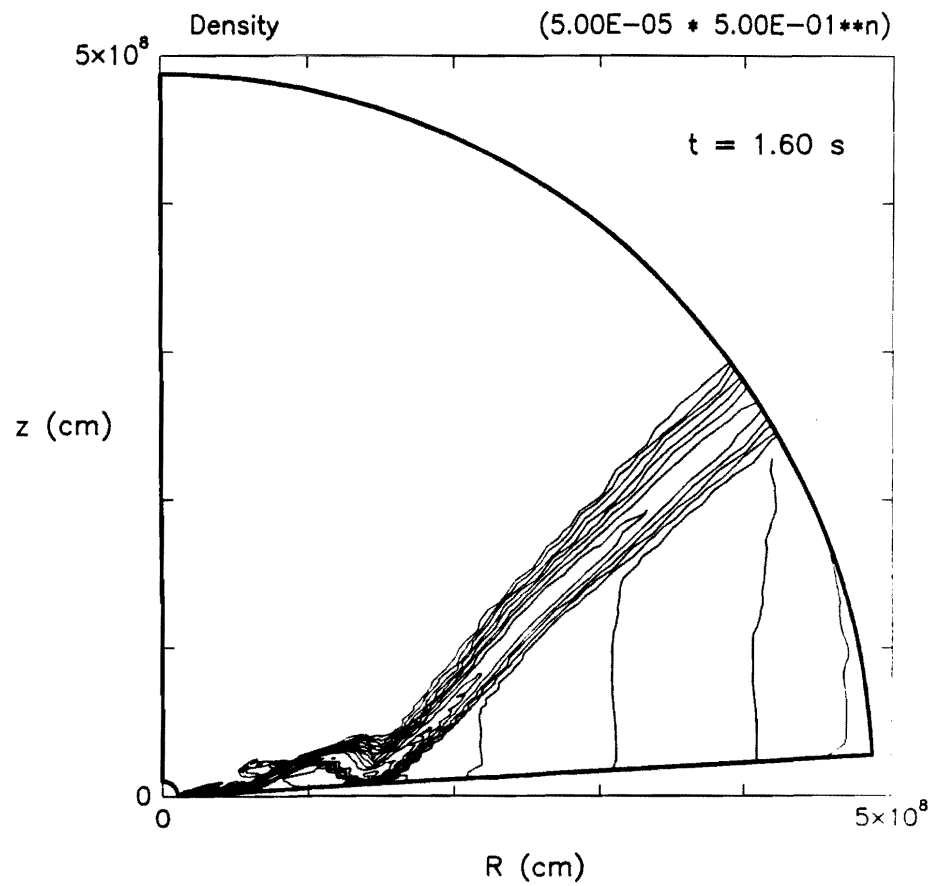

Figure 4(f)

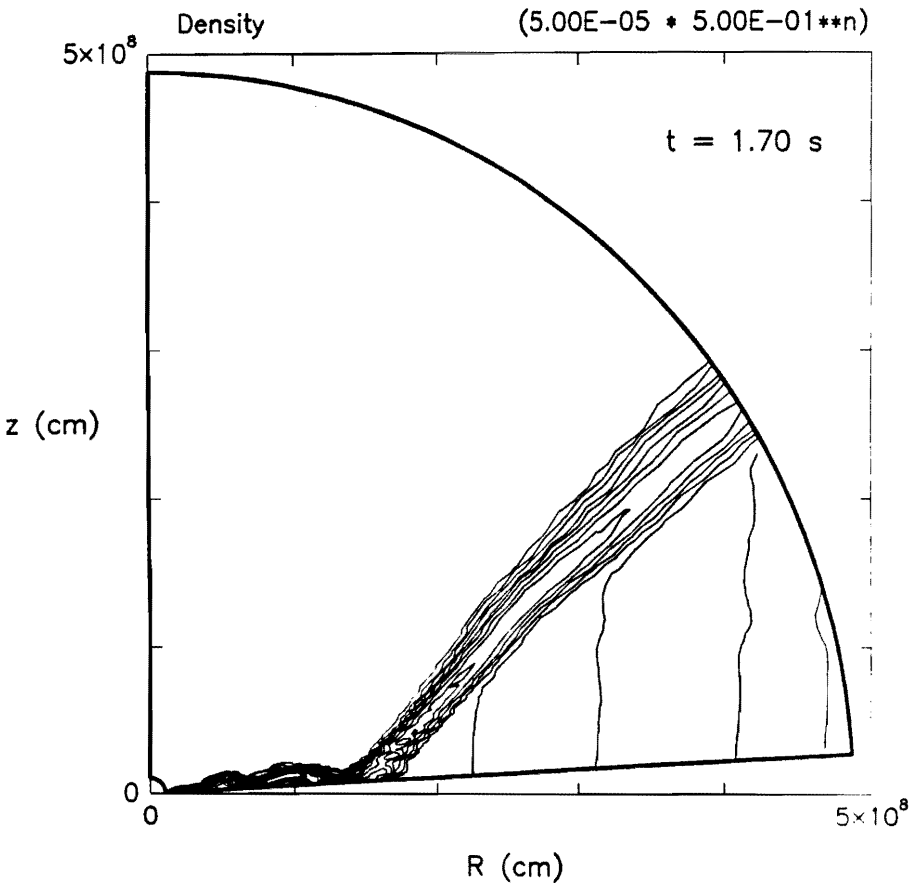

Figure 5(a)

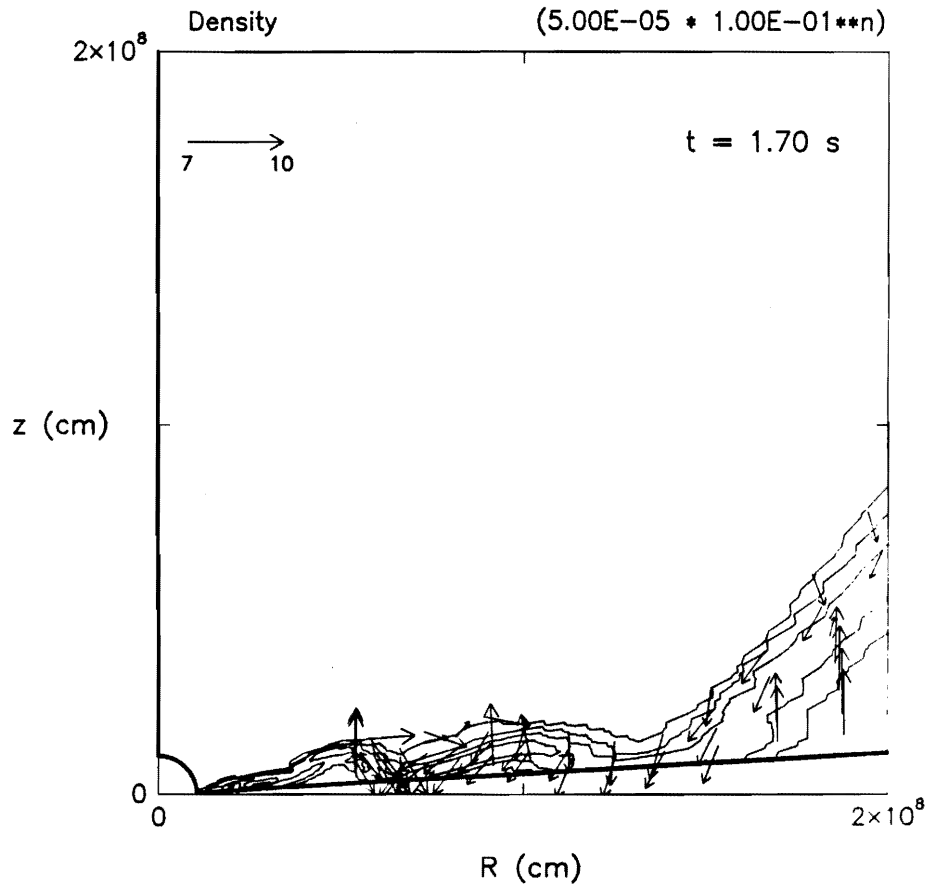

Figure 5(b)

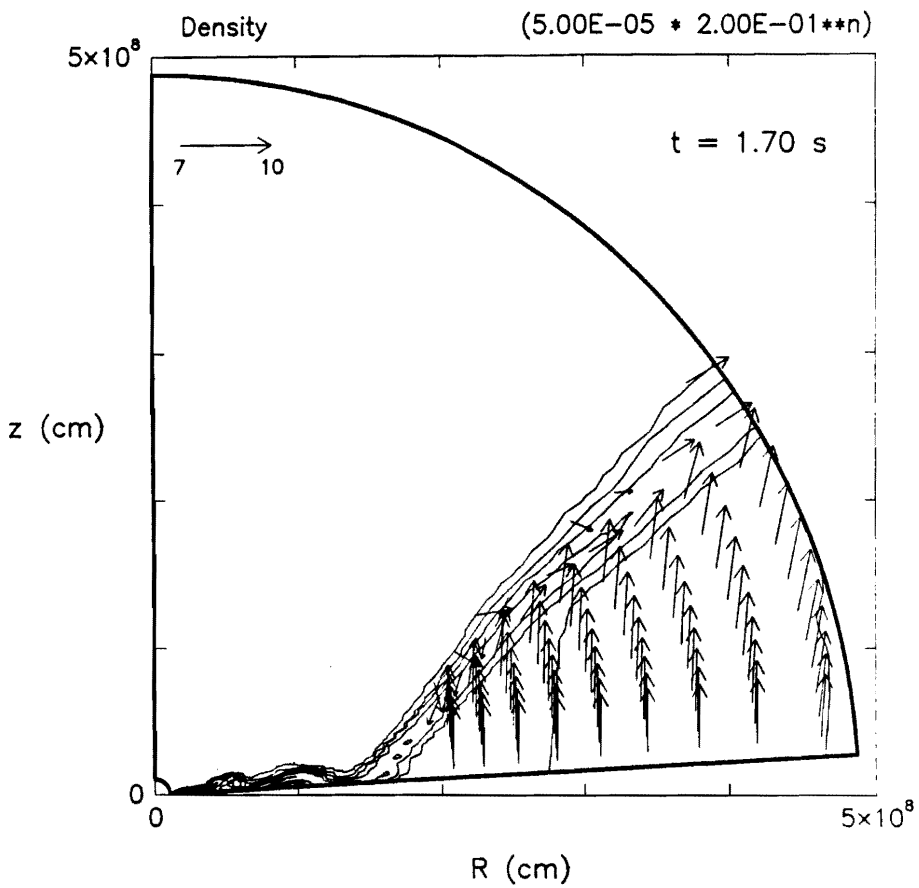

Figure 6

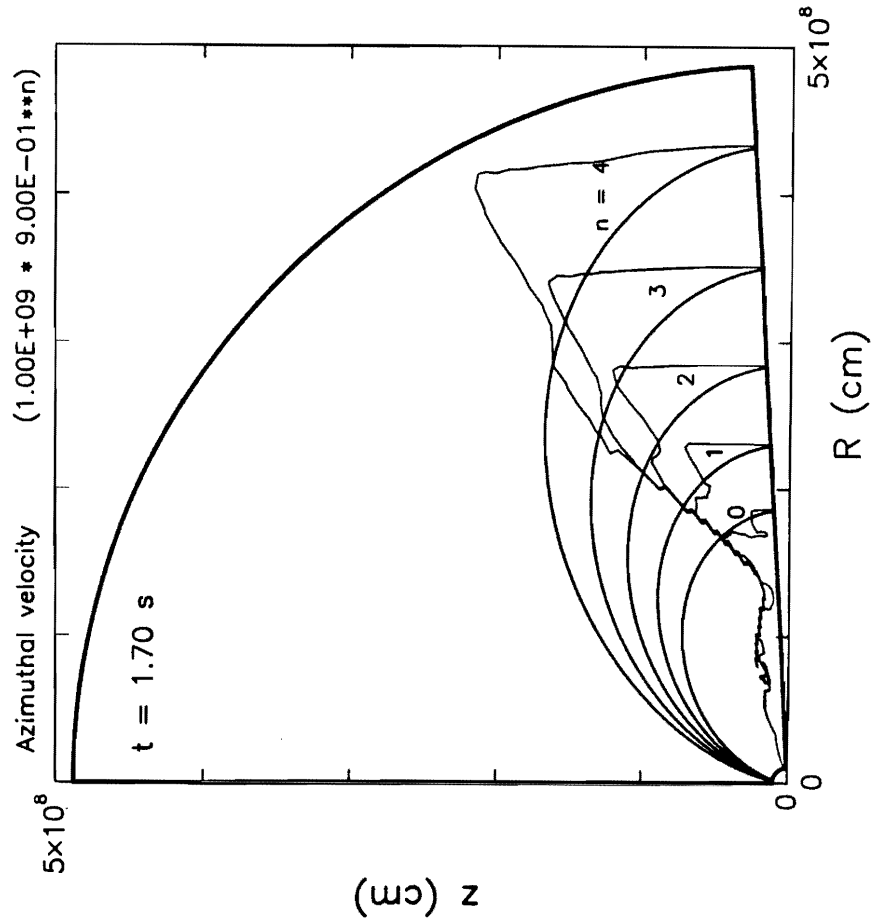

Figure 7(a)

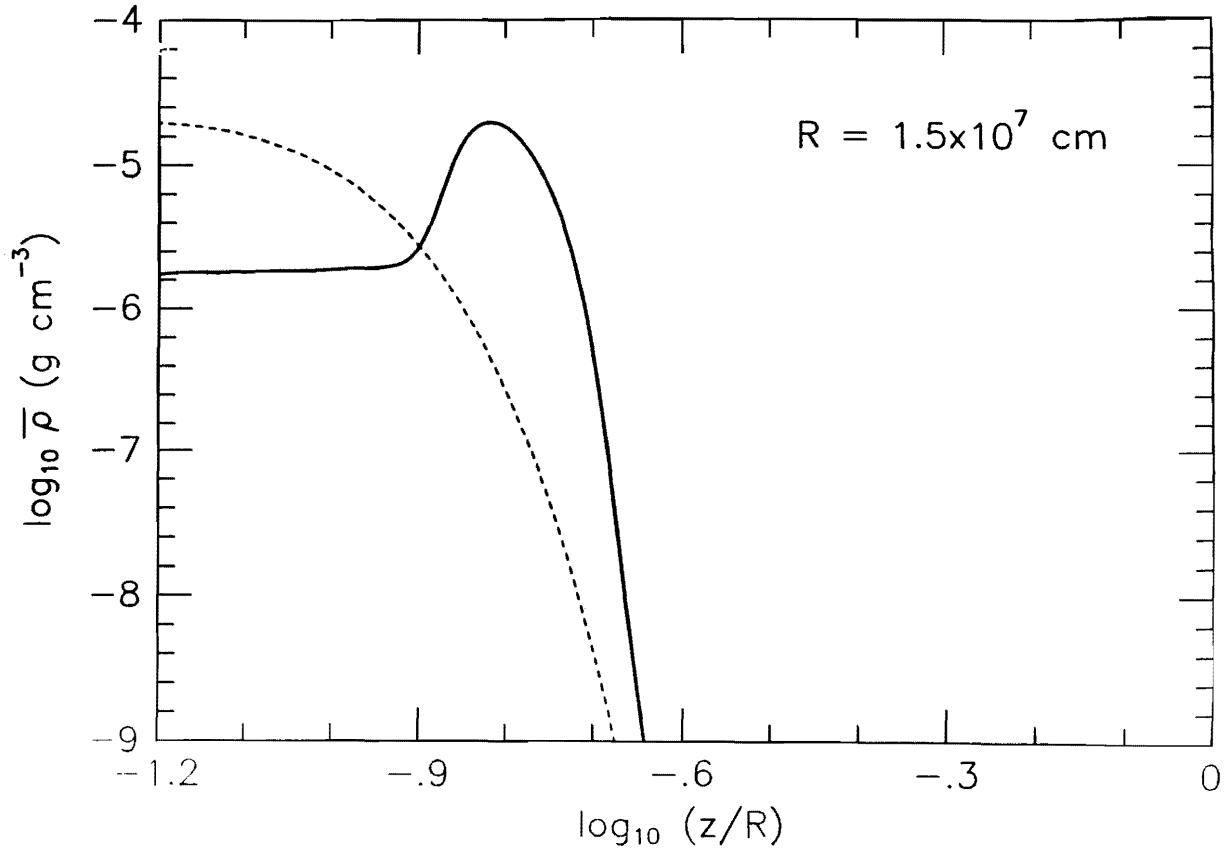

Figure 7(b)

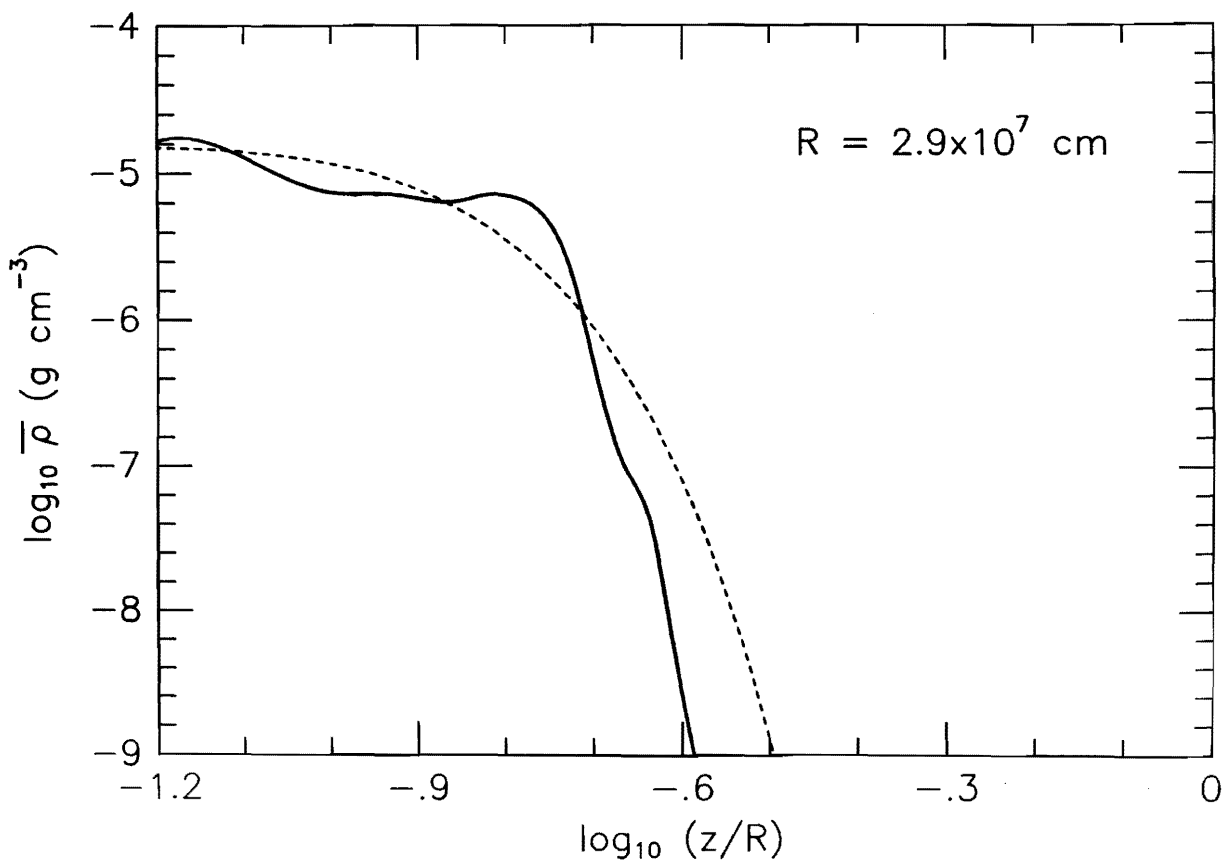

Figure 7(c)

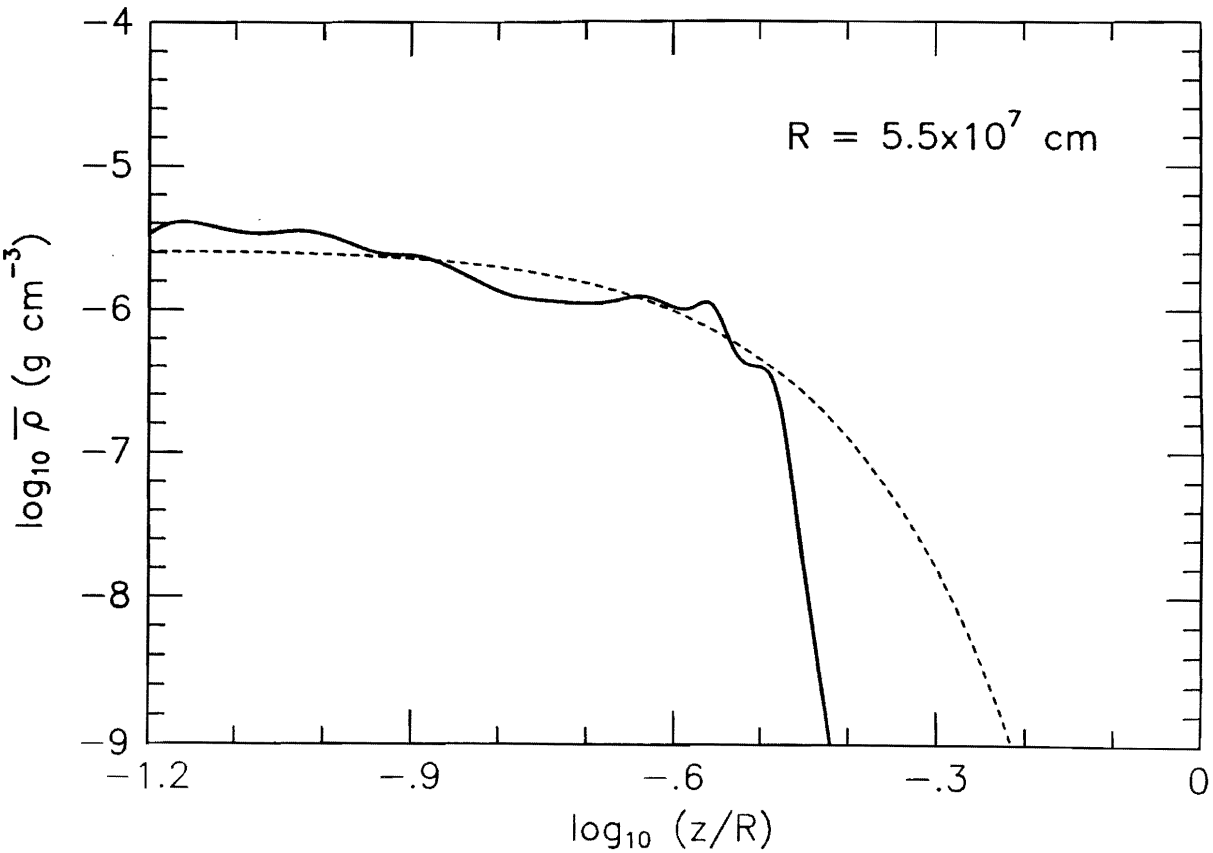

Figure 7(d)

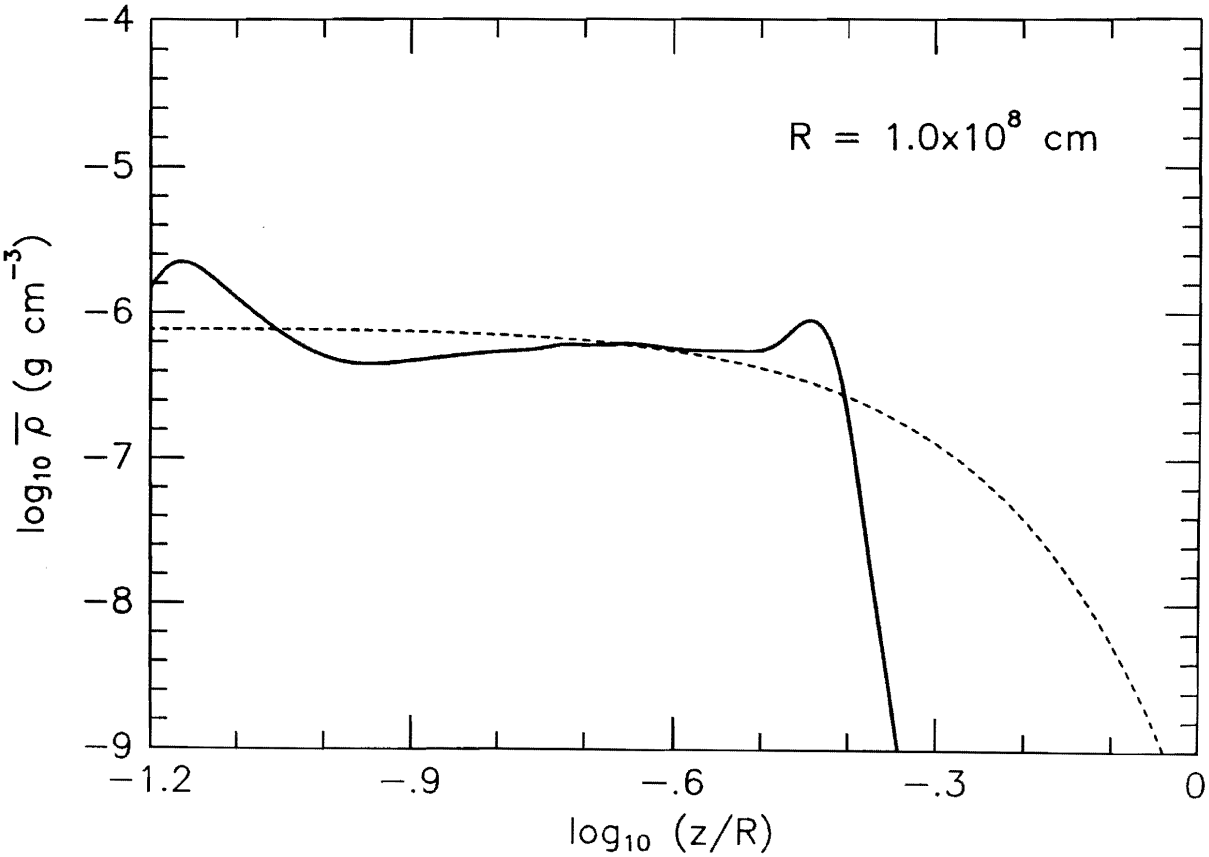

Figure 8

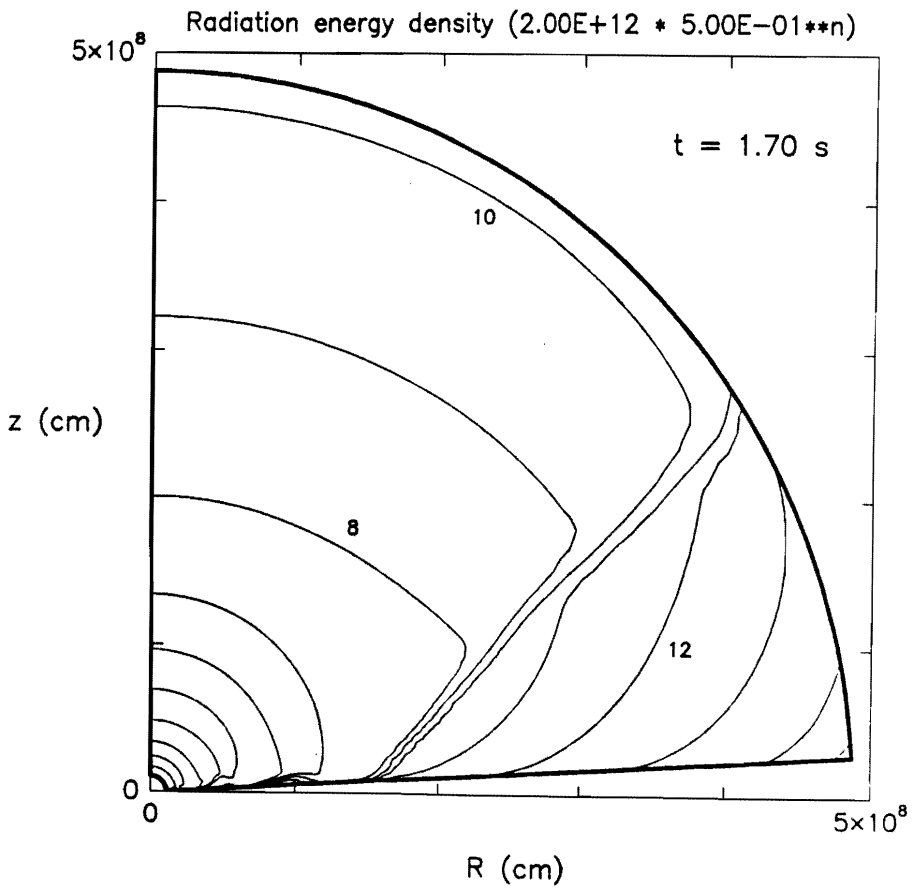

Figure 9

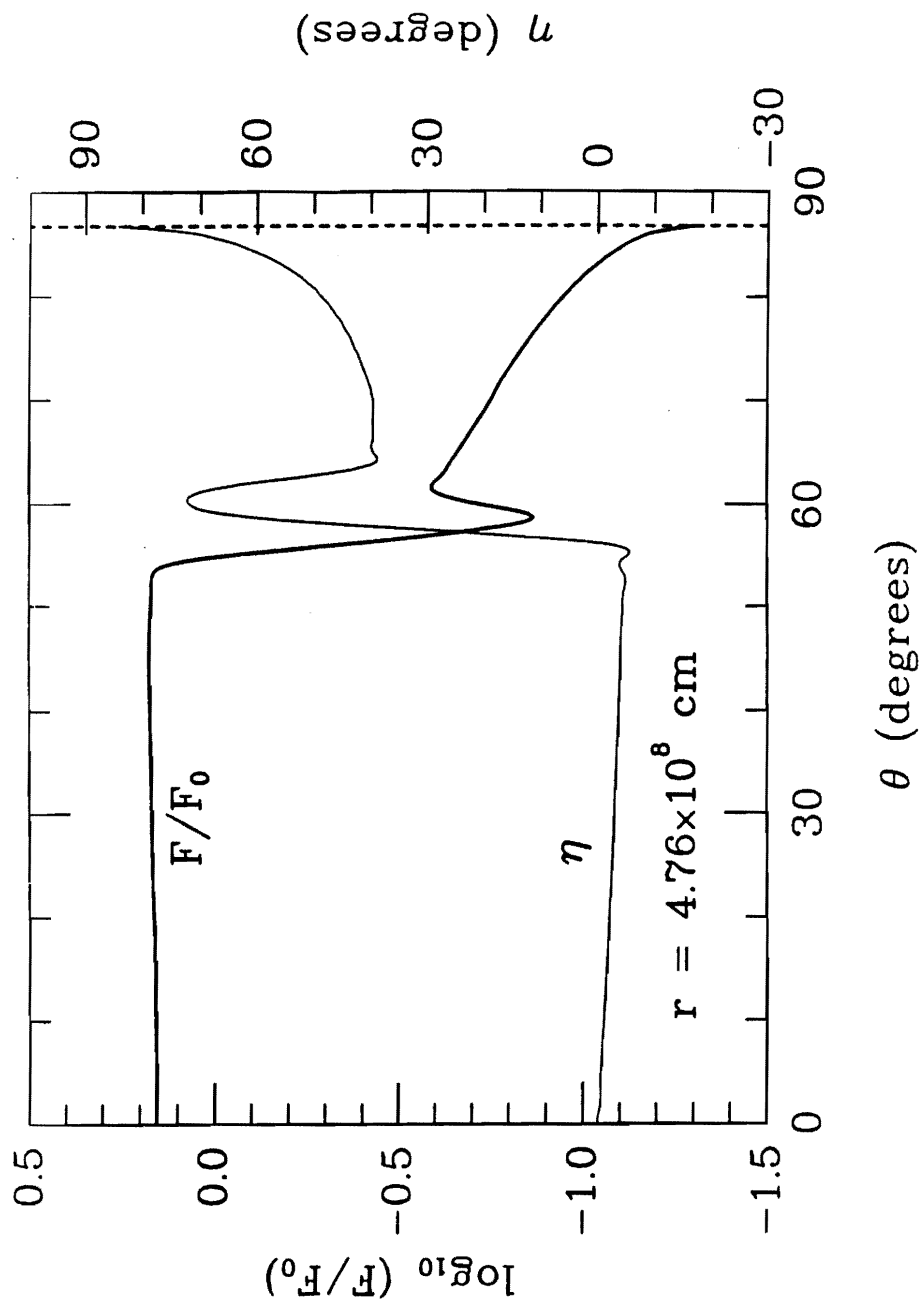

Figure 10(a)

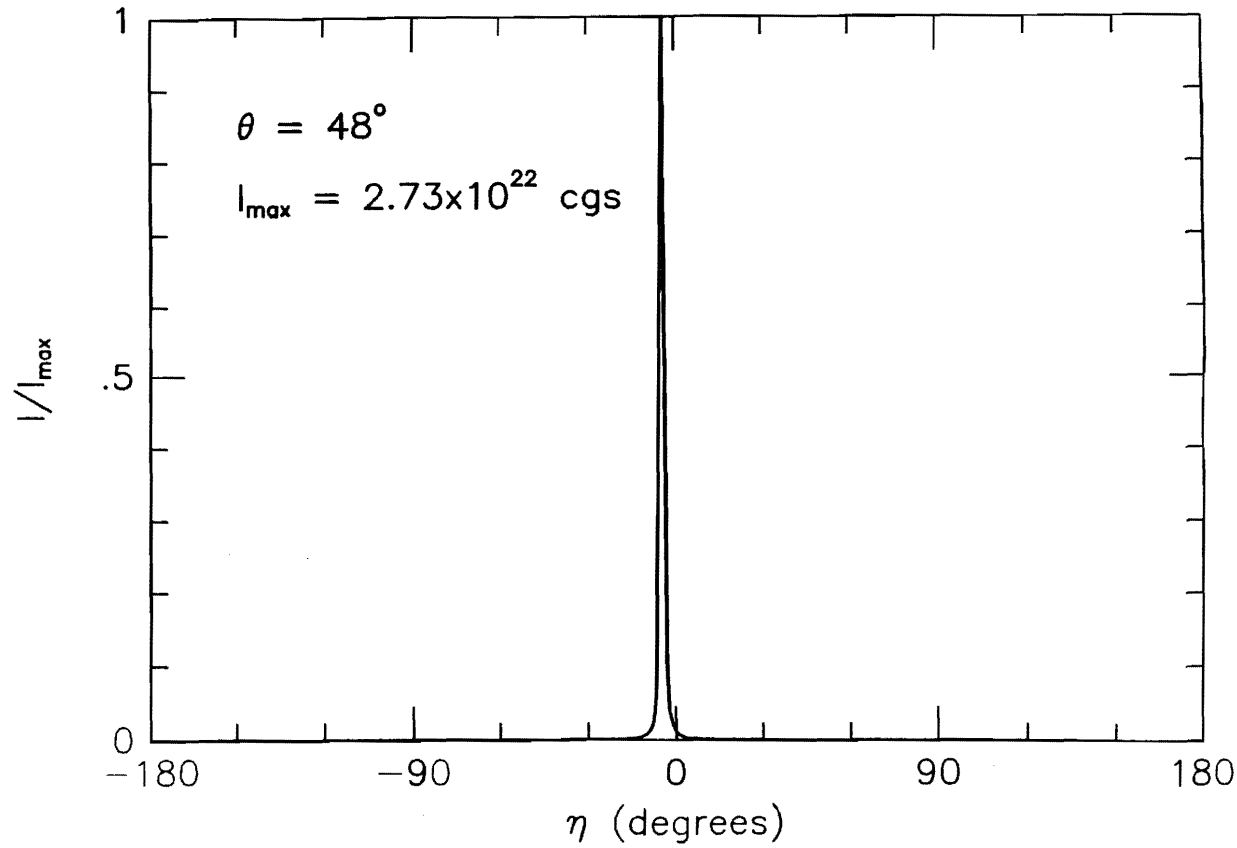

Figure 10(b)

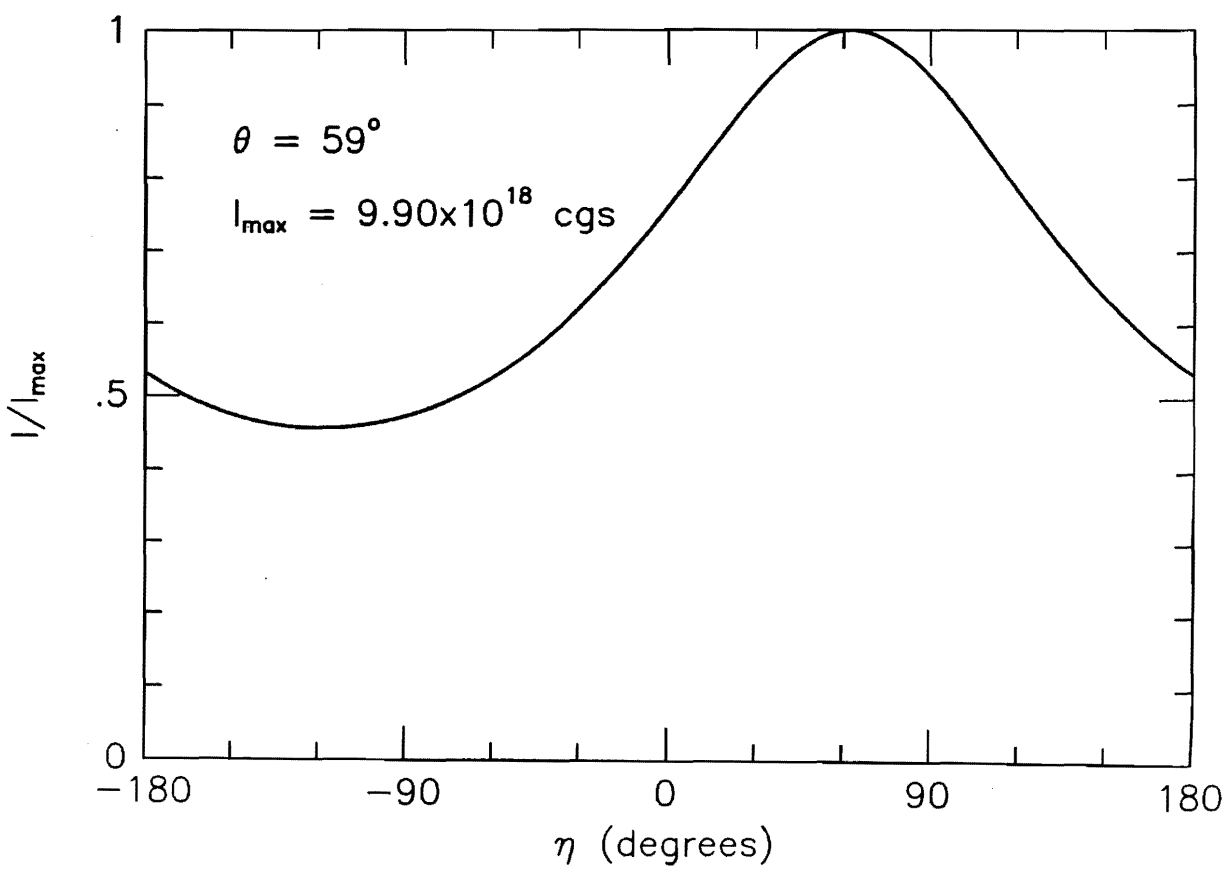

Figure 10(c)

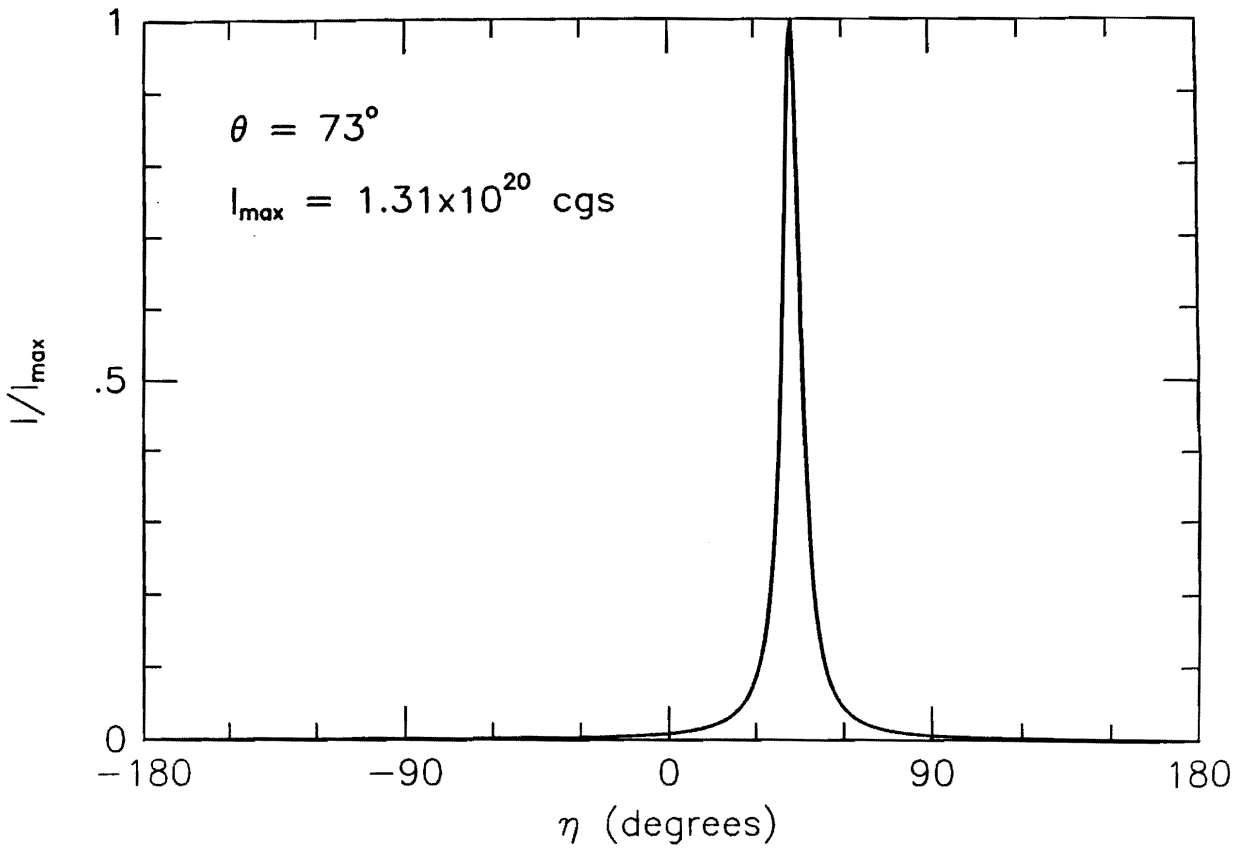

Figure 11

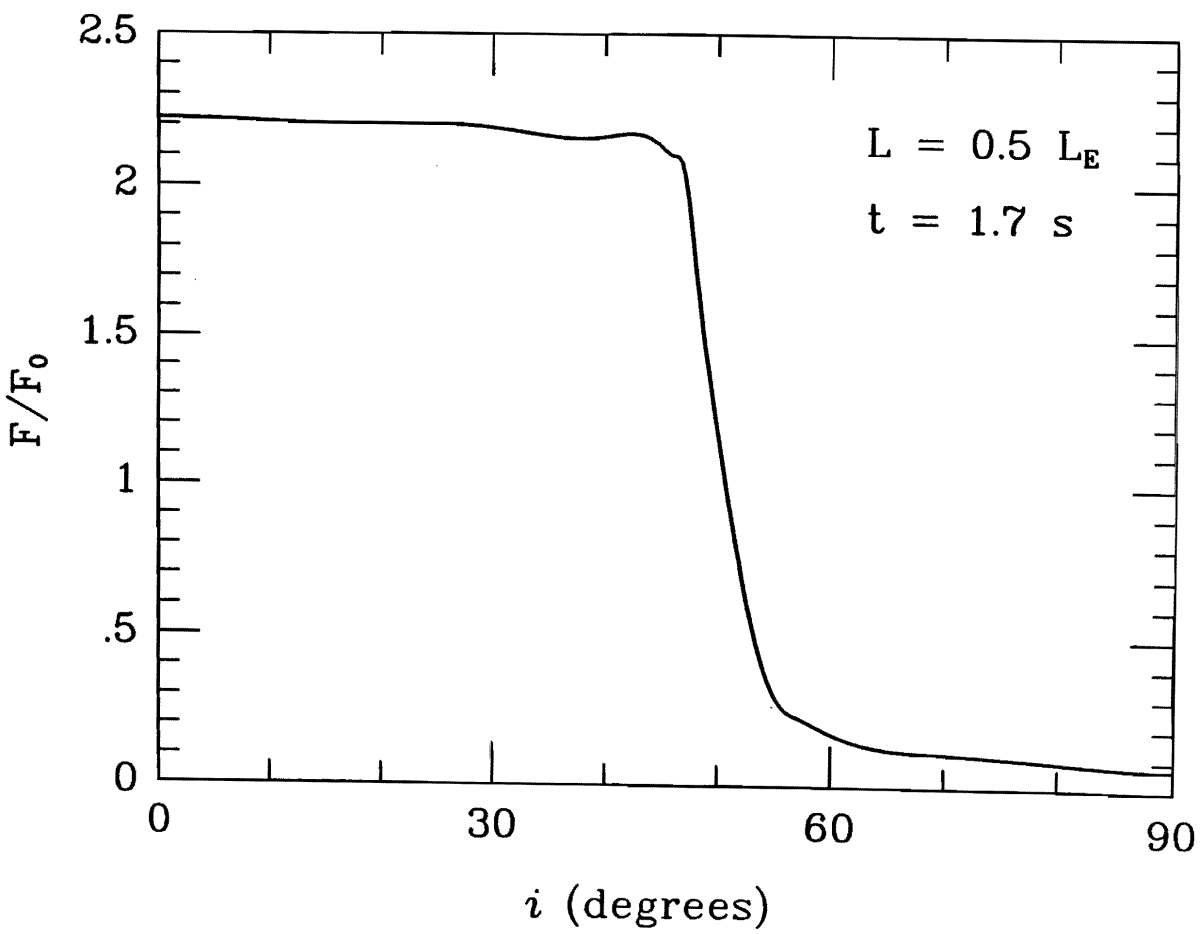

AUTHORS' ADDRESS:

Fulvio Melia,	**Department of Physics and Steward Observatory,**
	University of Arizona, Tucson, AZ 85721
	melia@nucleus.physics.arizona.edu
Gregory Zylstra	**Department of Physics,**
	University of Arizona, Tucson, AZ 85721